Environ Fluid Mech (2010) 10:499–520
DOI 10.1007/s10652-010-9181-0

ORIGINAL ARTICLE

Deducing an upper bound to the horizontal eddy diffusivity using a stochastic Lagrangian model

Daniel F. Carlson · Erick Fredj · Hezi Gildor · Vered Rom-Kedar

Received: 30 April 2009 / Accepted: 21 June 2010 / Published online: 14 July 2010

Abstract We present a method for estimating the upper bound of the horizontal eddy diffusivity using a non-stationary Lagrangian stochastic model. First, we identify a mixing barrier using a priori evidence (e.g., aerial photographs or satellite imagery) and using a Lagrangian diagnostic calculated from observed or modeled spatially non-trivial, time-dependent velocities [for instance, the relative dispersion (RD) or finite time Lyapunov exponent (FDLE)]. Second, we add a stochastic component to the observed (or modeled) velocity field. The stochastic component represents sub-grid stochastic diffusion and its mean magnitude is related to the eddy diffusivity. The RD of Lagrangian trajectories is computed for increasing values of the eddy diffusivity until the mixing barrier is no longer present. The value at which the mixing barrier disappears provides a dynamical estimate of the upper bound of the eddy diffusivity. The erosion of the mixing barrier is visually observed in numerical simulations,

Hezi Gildor—Formerly at The Environmental Sciences, Weizmann Institute of Science, Rehovot, Israel.

D. F. Carlson
Department of Environmental Science and Energy Research, Weizmann Institute of Science,
76100 Rehovot, Israel
e-mail: Daniel.Carlson@weizmann.ac.il

E. Fredj
Department of Computer Science, Jerusalem College of Technology, 21 Haavad Haleumi St.,
P.O. Box 16031, 91160 Jerusalem, Israel
e-mail: Fredj@mail.jct.ac.il
URL: http://molad.jct.ac.il/erick/ef/

H. Gildor (✉)
Institute of Earth Sciences, The Hebrew University of Jerusalem, Jerusalem, Israel
e-mail: hezi.gildor@huji.ac.il
URL: http://www.earth.huji.ac.il/people/hezi.asp

V. Rom-Kedar
Department of Computer Science and Applied Mathematics, Weizmann Institute of Science,
76100 Rehovot, Israel
e-mail: Vered.Rom-kedar@weizmann.ac.il
URL: http://www.wisdom.weizmann.ac.il/∼vered/

and is quantified by computing the kurtosis of the RD at each value of the eddy diffusivity. We demonstrate our method using the double gyre circulation model and apply it to high frequency (HF) radar observations of surface currents in the Gulf of Eilat.

Keywords Eddy diffusivity · Ocean mixing · Mixing barrier · Stirring · Turbulence · Parameterization · High Frequency radar

1 Introduction

A major challenge facing oceanographers is, and has consistently been, the observation, understanding, and modeling of ocean mixing (see, e.g. Stommel [1] and Burchard and Bolding [2]). The challenge persists today as mathematical approximations of mixing processes in ocean and climate models crudely represent very complex phenomena. Due to limited computing power, present-day ocean and climate models can only resolve mixing processes on scales down to a few tens of km, requiring the parameterization of smaller-scale processes. The effect of small-scale mixing processes is often modeled as "eddy diffusivity"—a diffusion-like term that is several orders of magnitude larger than the tracers' molecular diffusivity (see Majda and Kramer [3] for an extensive review).

Traditionally, geophysical mixing studies utilize either an Eulerian or a Lagrangian approach. The Eulerian approach decomposes the flow field into a stationary large-scale flow and a stochastic component, the formulation of which varies (see Sect. 7, Discussion for more detail). In these studies the large scale flow does not mix the particles—the mixing occurs only when the stochastic component is inserted. The Lagrangian approach utilizes dynamical systems methods (chaotic advection and Lagrangian coherent structures), emphasizing that a deterministic non-stationary large-scale flow (i.e. a non-trivial, temporally and spatially varying flow) mixes particles even when no stochastic component is introduced. The addition of a simple uncorrelated stochastic velocity component representing eddy mixing to such a flow results in the non-stationary, zeroth-order Lagrangian stochastic model. This model advects particles with a non-stationary large scale flow (obtained, for example, from a numerical ocean model or from high frequency (HF) radar-derived surface current maps) and attempts to include turbulent sub-grid-scale effects through the incorporation of a random variable whose magnitude usually has some dependence on the eddy diffusivity (see, e.g., Ross and Sharples [4]). With the advancement of oceanographic monitoring systems and high resolution numerical ocean models the non-stationary, zeroth-order Lagrangian stochastic model has been used in various applications, including the study of pollution dispersion [5,6], larval dispersion [7–10], and entrainment of power plant outflows [11].

Our goal is to provide an estimate for an upper bound to the eddy diffusivity K, used to parameterize sub-grid, unresolved ocean mixing processes. As noted by Davis [12], K is a diagnosed (or observed) parameter that depends on the flow, and simple scaling arguments yield a wide range of possible values (see Sect. 5). Previous studies have estimated K through dye releases [13–15], drifter trajectories [16–18], and mathematical theory coupled with observations [19] but extracting the value of K is not trivial. We propose a dynamical method to estimate an upper bound for K by examining how Lagrangian barriers present in a deterministic large-scale flow are destroyed by adding eddy diffusivity.

Roughly speaking, by 'barrier' we mean a line that separates regions with different mixing characteristics with little mixing across this line. For a precise formulation see Haller and Yuan [20] and Haller [21] (and references therein). Mixing barriers are common in geophysical flows [22–36]. Barriers deform and change their location in time [37] and appear to be robust to uncertainties in the large-scale flow [38] (see also Sect. 5) and to sufficiently weak sub-grid fluctuations (see Sects. 4, 5). In other words, barriers can be diagnosed even if the large-scale flow contains various sources of uncertainties. As a result of small-scale processes, mixing barriers are semi-permeable [37].

Our proposed method to estimate the upper bound of K starts with an independently verified mixing barrier (from aerial photographs or from satellite imagery). The existence of the barrier is then established by calculating the relative dispersion (RD) of passive particles advected by the observed or modeled non-stationary flow (see, for instance, Boffetta et al. [24]; Orre et al. [27]; Gildor et al. [35]). In reality, tracers are affected by both the large-scale flow and also by small-scale processes that are not observed or resolved by deterministic numerical models or by observational systems. Therefore, we then assume that the local velocity field consists of an observed non-stationary large-scale flow (with non-trivial spatial and temporal dependence) and unknown or unresolved sub-grid processes, represented by a stochastic fluctuating component. The stochastic component is related to the eddy diffusivity, K, and we increase the magnitude of K until the mixing barrier is no longer present. The eradication of the mixing barrier by the eddy diffusivity can be seen visually by plotting the RD and is quantified by calculating the kurtosis of the RD computed for each value of K. In other words, the magnitude of K that eradicates the mixing barrier provides an estimate of the upper bound of the horizontal eddy diffusivity.

The structure of this paper is as follows: in Sect. 2 we review some methods for identifying mixing barriers in deterministic, time-dependent velocity fields and demonstrate them using the idealized, extensively studied example of the double gyre. Section 3 introduces the non-stationary, zeroth-order Lagrangian stochastic model. In Sect. 4 we apply the non-stationary, zeroth-order Lagrangian stochastic model to the double gyre and use our proposed method to demonstrate the sensitivity of the mixing barriers to the eddy diffusivity, thus deducing an upper bound to the eddy diffusivity. Section 5 applies our method to observations of a mixing barrier in the Gulf of Eilat. We evaluate the sensitivity of our method in Sect. 6 and we discuss our results and conclude in Sects. 7 and 8, respectively.

2 Deterministic Lagrangian model

Mixing barriers in passive scalar fields are apparent to the eye. Yet, the exact mathematical formulation of the existence of such barriers is non-trivial and has been the subject of extensive research over the last decade [24,38]. The double gyre kinematic model became a classical paradigm for studying such barriers (see the Lagrangian Coherent Structures tutorial http://www.cds.caltech.edu/~shawn/LCS-tutorial/contents.html and references therein). The stream function

$$\psi(x, y, t) = A \sin(\pi f(x, t)) \sin(\pi y) \tag{1}$$

$$f(x, t) = a(t)x^2 + b(t)x \tag{2}$$

$$a(t) = \varepsilon \sin(\omega t) \tag{3}$$

$$b(t) = 1 - 2\varepsilon \sin(\omega t) \tag{4}$$

of the double gyre is stationary for $\varepsilon = 0$ and time-periodic for $\varepsilon > 0$. Equations 1, 2, 3, 4 confine particles to the physical domain [0,2] × [0,1] and the velocities are defined, in terms of the stream function (1), as

$$u = -\frac{\partial \psi}{\partial y} = -\pi A \sin(\pi f(x,t)) \cos(\pi y) \tag{5}$$

$$v = \frac{\partial \psi}{\partial x} = \pi A \cos(\pi f(x,t)) \sin(\pi y) \frac{\mathrm{d}f}{\mathrm{d}x} \tag{6}$$

The following parameters were used in all the double gyre numerical simulations:

$$\omega = \frac{2\pi}{T}; \quad A = 0.1; \quad \varepsilon = 0.25,\ 0; \quad T = 10; \quad \mathrm{d}x = \mathrm{d}y = 0.005; \quad \mathrm{d}t = 0.01$$

ω is the frequency of oscillation, T is the tidal period, and A represents the amplitude of the velocity vectors. ε is a measure of how far the separation line between the gyres moves from left to right, specifying the magnitude of motion of the separation point. The grid spacing, represented by $\mathrm{d}x$ and $\mathrm{d}y$, is constant as is the time step, $\mathrm{d}t$. The time-periodic double gyre ($\varepsilon = 0.25$) and the stationary double gyre ($\varepsilon = 0$) are examined to highlight the differences between the mixing characteristics of time-dependent and stationary flows (see Sect. 4). The simulations were integrated over the time interval $t = [0, 17]$. All variables and parameters are dimensionless, yielding a dimensionless estimate of the upper bound of the eddy diffusivity (see Sect. 4).

Figure 1 shows the velocity field for the time-periodic double gyre at times t =1 (a) t =7 (b). The flow field of the stationary double gyre at all times is shown in Fig. 1a.

The model velocity field is used to calculate virtual particle trajectories by integrating:

$$\frac{\mathrm{d}x_k}{\mathrm{d}t} = u\,(x_k, y_k, t)\,; \quad \frac{\mathrm{d}y_k}{\mathrm{d}t} = v(x_k, y_k, t) \tag{7}$$

The subscript k denotes the index of each particle ($k = 1, \ldots, N$; N is the total number of particles), and u and v are the zonal and meridional velocity components, respectively. To enable a direct comparison with the Lagrangian stochastic model in Sect. 3, we use the simple forward Euler–Maruyama method to perform the integration. The time step is sufficiently small so that the forward Euler–Maruyama method produces the same result as the fifth order Runge–Kutta (for the deterministic case). The Eulerian velocity field is computed using the streamfunction and then linearly resampled in space and time to examine the applicability to real-life geophysical examples where the velocity field is measured or observed only at discrete times and spatial locations.

Several statistical measures have been proposed to characterize the dispersion of particles under a given velocity field. These include the RD and the maximum Lyapunov exponent (MLE), which is approximated by the largest finite time Lyapunov exponent (FTLE) or finite size Lyapunov exponent [24–27].

The RD is calculated using thousands of evenly distributed particles within a domain. For each particle, initially located at $z_k(0) = (x_k, y_k)$ the average squared RD of its four nearest neighbors from its own location at time t is

$$\mathrm{RD}_k^2(t) = \frac{1}{4} \sum_{j=1}^{4} \big(z_j(t) - z_k(t)\big)^2. \tag{8}$$

The RD field at time t shows the value of the RD at each grid point (e.g. column I of Figs. 3, 4).

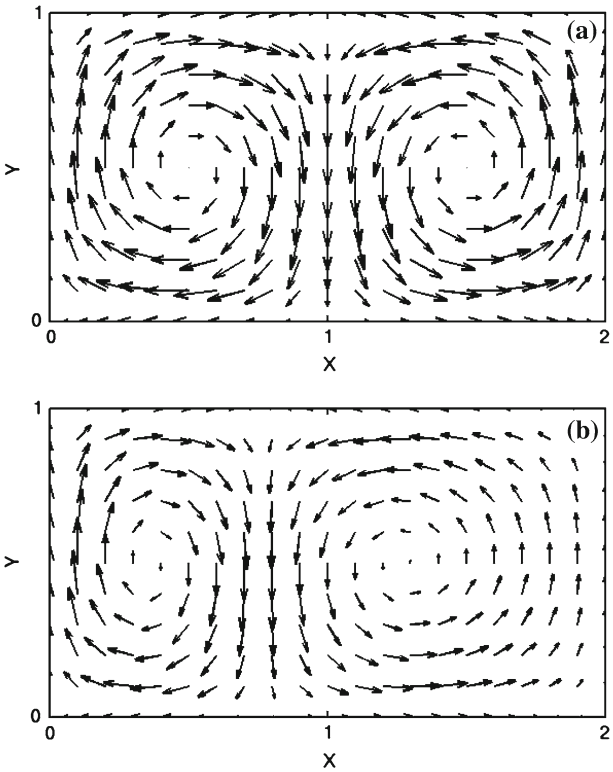

Fig. 1 The initial velocity field for the time dependent double gyre model described in Sect. 2 at **a** $t = 0$ and at **b** $t = 7$. All variables are dimensionless. An *animation* showing the time dependence of the circulation can be viewed online: http://www.cds.caltech.edu/~shawn/LCS-tutorial/examples.html#Sec7.1

Another common approach for studying the mixing and chaotic properties of dynamical systems [39–41], involves the calculation of the MLE, λ. The MLE provides the common rate of exponential separation of two nearby trajectories and is defined as

$$\lambda = \lim_{t\to\infty} \lim_{\delta(0)\to 0} \frac{1}{t} \ln\left(\frac{\delta(t)}{\delta\,(0)}\right) \tag{11}$$

where

$$\delta(t) = \|z_1(t) - z_2(t)\| \tag{12}$$

is the distance between two typical trajectories at time t. $\lambda > 0$ indicates hyperbolic trajectories (nearby trajectories separate at an exponential rate). The FTLE field is found by calculating a finite approximation to λ. The FTLE and the RD fields shown in Fig. 2 produce similar images for sufficiently fine grids. In these images, mixing barriers appear as "ridges" or lines of local maximal stretching [20,27].

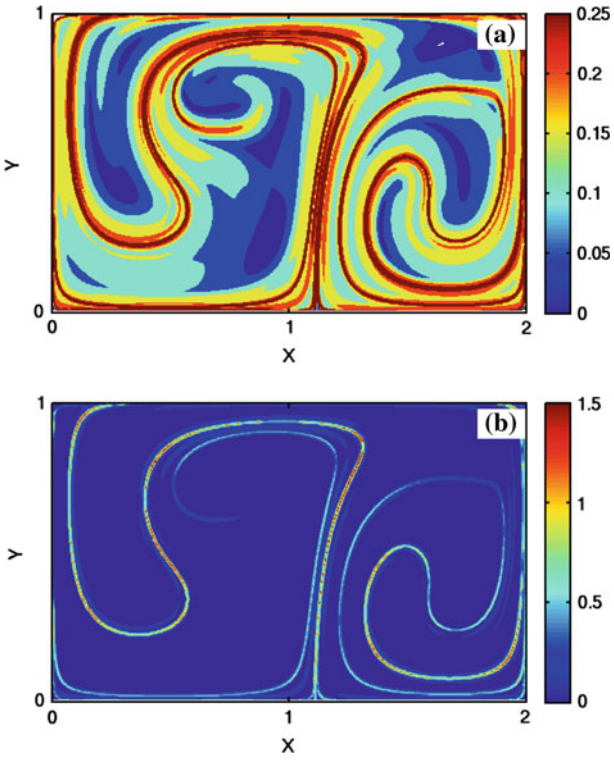

Fig. 2 Comparisons of the FTLE (**a**) and the RD (**b**) show similar barrier structures in the deterministic time-dependent double gyre case

3 Stochastic Lagrangian model

While the deterministic non-stationary models provide a qualitative explanation of mixing patterns in the ocean [40,41], in real life there are sub-grid processes that are not resolved by observational systems or by numerical models. In climate models, the ocean model does not usually resolve the submesoscale processes (1–10 km) as these models use grid sizes of ∼O(100 km). Regional ocean models that use grid sizes of ∼O(1 km), resolve these processes, yet do not resolve smaller scale fluctuations. To represent the possible effects of these processes, the Lagrangian model introduced in Sect. 2 is modified to include a stochastic component. The stochastic term influences the form and existence of the barriers and enables us to deduce an approximate upper bound to the eddy diffusivity.

The problem of describing the statistical transport of passive tracers by the Eulerian approach may be formulated by prescribing a velocity field $\mathbf{u}(\mathbf{x}, t) = \overline{\mathbf{u}} + \mathbf{u}'$. This seemingly simple formulation relies on the implicit assumption that the large and small scale motions are clearly separated in wave number/time frequency domain and that $\mathbf{u}'$ may be adequately described by some stochastic process [42]. In oceanic flow, this is not always the case [42,43]. Additionally, the decomposition of the flow is not straightforward [44]. For instance, $\overline{\mathbf{u}}$ could represent an hourly, daily, or seasonal mean and the grid size over which it is calculated affects $\overline{\mathbf{u}}$ [12,45]. The temporal and spatial averaging techniques that are used to calculate $\overline{\mathbf{u}}$ influence the statistical characteristics of $\mathbf{u}'$ [1].

In the Lagrangian approach (used in the present study) we replace $\overline{\mathbf{u}}$ with $\mathbf{U}_{LS}$: the observed or simulated large scale flow with spatial and temporal variability, instead of a constant mean. Additionally, we define $\mathbf{u}'$ as a random fluctuation with prescribed statistics representing turbulent or other unresolved, disordered fluctuations (see, for example Sect. 3 of Ullman et al. [46]). The crucial requirement is that $\mathbf{U}_{LS}$ allows the mixing barrier to be diagnosed (this may not be the case if, for example, time averaging is performed over periods much longer than the typical life time of such a barrier). Thus, $\mathbf{U}_{LS}$ in our HF radar observations (see Sect. 5) represents a sort of average over 30 min and over a grid size of 300 by 300 m. In the case of the flow derived from the stream-function (Eqs. 1–4), $\mathbf{U}_{LS}$ is taken to be a sort of "snapshot" of the velocity field at a specific time, but it is very similar to the averaged velocity over the same time interval. Here, the time step between each "snap-shot" is much smaller than both the time required for a particle to traverse a gyre and the period of the perturbation.

It is important to note the difference between the non-stationary zeroth-order Lagrangian stochastic model employed here and the more traditional stationary zeroth-order Lagrangian stochastic model (see LaCasce [45] for a review). The main difference between the two models is the use of a non-stationary large scale flow with implications on the magnitude of the eddy mixing coefficient. If one neglects the role of chaotic stirring and tries to find an eddy mixing coefficient to explain observed dispersion of passive tracers, the mixing coefficient due to turbulent mixing becomes larger [33]. In the next section we address this difference using the double-gyre example, demonstrating the importance of adequate temporal resolution of the "large scale" flow. The non-stationary zeroth-order Lagrangian stochastic model (13) has become popular in recent oceanographic and limnological applications [4–11].

We seek to describe the trajectory $\mathbf{X}(t)$ of a particle released initially at x_0 and transported jointly by the flow $\mathbf{U}_{LS}$ and a fluctuating stochastic component $\mathbf{u}'$, which roughly represents the eddy diffusion. The equation for the trajectory is a (vector-valued) stochastic differential equation [47]

$$dX(t) = \mathbf{U}_{LS}(\mathbf{X}(t), t)\, dt + \sqrt{2K\, dt}\, dw(t); \quad X(t=0) = x_0. \tag{13}$$

In (13) $\mathbf{U}_{\mathrm{LS}}$ represents the large-scale time-dependent velocity, K is the eddy diffusivity, and w is a random number derived from a zero-mean, white noise Gaussian distribution [47].

As in the deterministic case, we track the trajectories of multiple particles simultaneously. Each of the trajectories individually obeys (13) with the same deterministic velocity field $\mathbf{U}_{LS}(\mathbf{x}, t)$, but with independent Brownian motions. The integration method and interpolation methods are the same as those described in Sect. 2.

While the stream function (Eqs. 1–4) confines the particle trajectories to the domain, the addition of the stochastic term enables the particles to encounter the boundaries requiring boundary conditions to be set. If a stochastic "jump" results in a particle reaching a boundary, that particle is temporarily "stuck" on the boundary. Particles on the boundary may enter the flow field in future time steps through stochastic motion. The boundary conditions are analogous to floating debris deposited on a beach by waves and possibly swept back out to sea at a later time.

4 Toy model application: the double gyre

The double gyre model introduced in Sect. 2 is used to demonstrate the proposed method. We present the mixing characteristics of the time-periodic and stationary double gyre cases in Figs. 3 and 4. Row (a) presents the results for zero diffusivity and rows (b)–(d) present

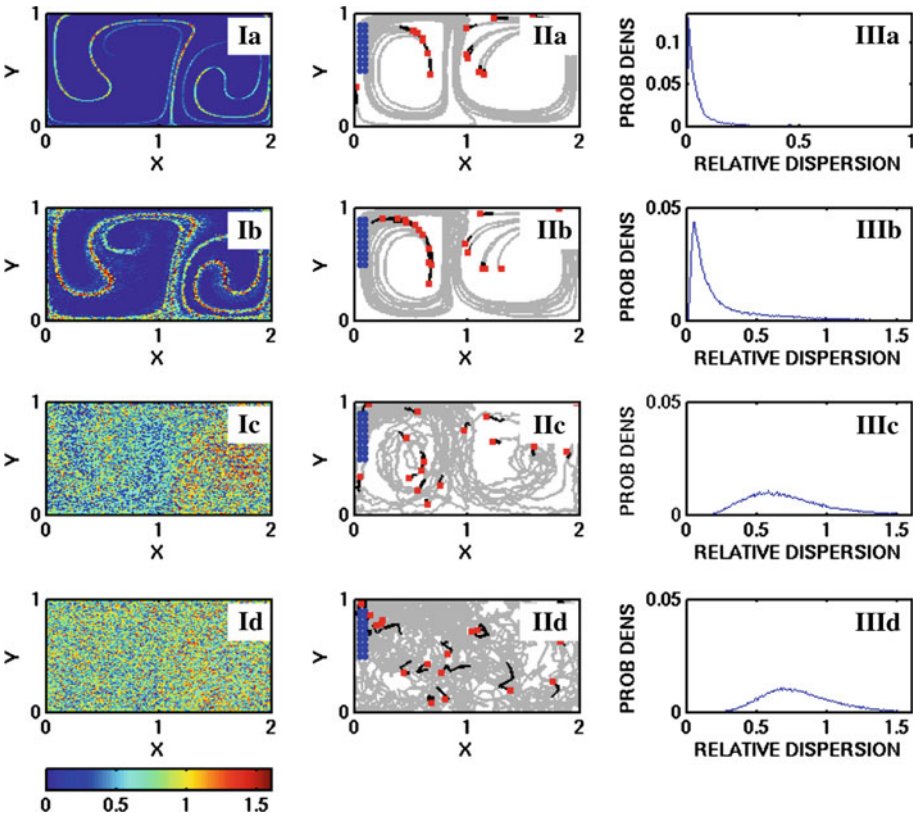

Fig. 3 Relative dispersion, particle trajectories, and PDFs of the RD are shown for the time-periodic double gyre model. Row (a) represents the deterministic case, i.e. $u' = 0$. Rows (b)–(d) show results for $K = \{10^{-5}, 10^{-3}, 10^{-2}\}$. The domain size and the RD are dimensionless. *Column I* High values of the RD indicate the presence of mixing barriers. *Column II* The increasingly random nature of the trajectories and the degradation of the mixing barrier are evident as K increases. Particle trajectories begin at the *blue circles*. The *gray lines* represent the trajectory, the *black lines* the final six positions, and the *red squares* indicate the final position. *Column III* Probability density functions of the RD show the broadening of the peak as the RD becomes more spatially uniform with increasing K

results for increased diffusivity. Column I shows the RD, used here to visually identify the barriers. Regions of large RD, displayed as contours of warm colors, represent barriers to mixing. Column II shows several particle trajectories and column III shows the probability density functions (PDFs) of the RD.

Contour plots of the RD for increasing K show the degradation of the mixing barrier (Column I, Figs. 3, 4). In panel Ia of Figs. 3 and 4, the high values of RD that represent mixing barriers are concentrated along thin lines. However, as K increases the thin barriers become blurred (panels Ib–Id) indicating increased dispersion by the eddy diffusivity. For $K = 10^{-5}$ (panel Ib, Figs. 3, 4) the barriers are still seen, whereas at $K = 10^{-3}$ (Panel Ic, Figs. 3, 4) the barriers cannot be easily detected and are not visible at $K = 10^{-2}$ (Panel Id, Figs. 3, 4).

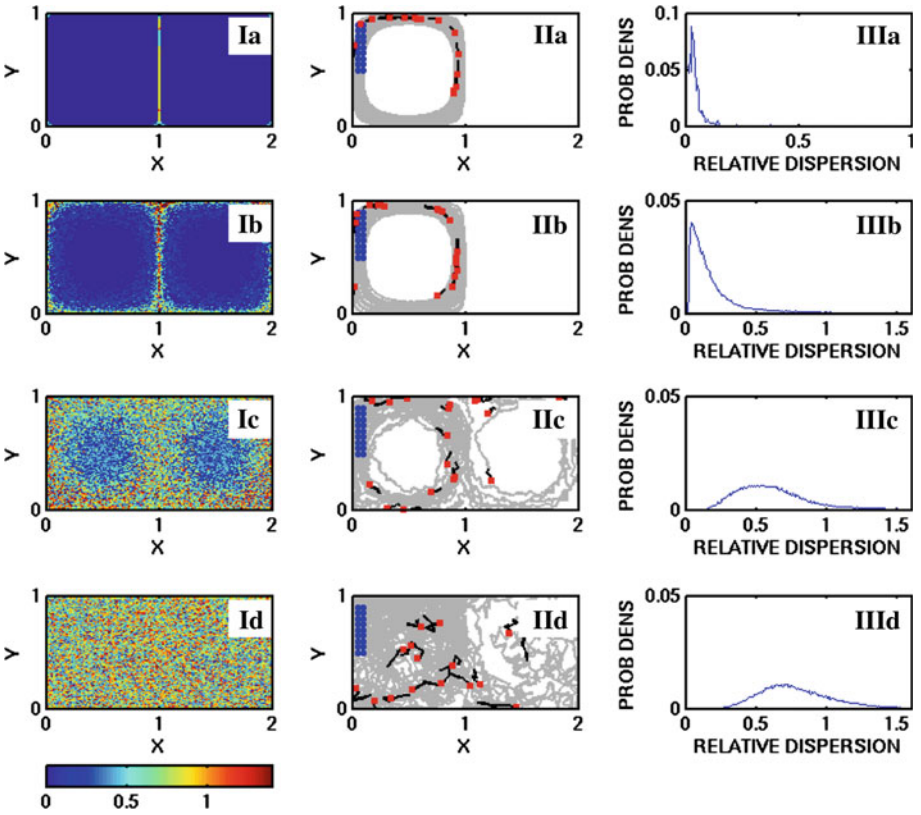

Fig. 4 The same as Fig. 3, but for the stationary double gyre

4.1 Stationary versus time-dependent mixing

Comparison of panel Ia in Figs. 3 and 4 demonstrates the differences in the structure and spatial distribution of the barriers of the time-periodic and stationary double gyre for $K = 0$. For the stationary case, there is a single barrier of finite length and constant location, whereas for the time-periodic case, the length of the barriers increases with time (not shown) and the barrier locations evolve periodically in time. These differences affect the degradation of the barriers with increasing K, as is evident when comparing panel Ic of Figs. 3 and 4. While the separation into two gyres is seen in the stationary case (panel Ic of Fig. 4), the gyres are hardly seen in the time-dependent case (panel Ic of Fig. 3).

The difference between the stationary and time-periodic cases can also be seen by following example trajectories (Column II, Figs. 3 and 4). At $K = 0$ (panel IIa) all particles remain within the left gyre in the stationary case (Fig. 4), whereas several particles were entrained into the right gyre in the time-periodic case (Fig. 3). All particle trajectories began at the same initial positions (left side of the domain, indicated by the blue circles). As K increases, particles can cross the barriers in both the stationary and time-periodic cases and the separation between nearby particles increases. In both cases, when K increases to 10^{-2} the double gyre circulation pattern is not evident in the particle trajectories—their end positions appear

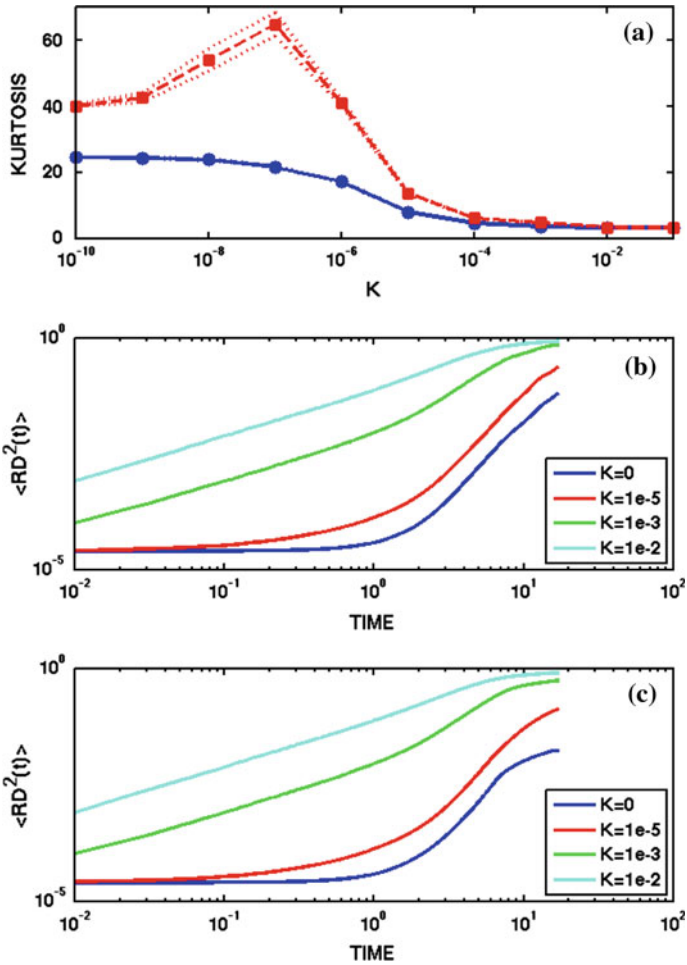

Fig. 5 **a** The ensemble average kurtosis of the RD is plotted as a function of the eddy diffusivity K for the time-dependent double gyre (*solid blue line*) and the stationary double gyre (*dashed red line*). The *dotted blue* and *red lines* show the standard deviation about the mean for the time-periodic and stationary double gyre cases, respectively. K is plotted on the x-axis using a logarithmic scale. The estimated upper bound for K in the time-periodic double gyre is 10^{-3}. The estimated upper bound for K in the stationary double gyre is 10^{-2}. **b** The logarithm of the domain averaged RD^2 as a function of time for given K (corresponding to the four values of K shown in Figs. 3 and 4) for the time-periodic double gyre. **c** The same as for (**b**), but for the stationary double gyre. The slope of the two *upper curves* in both (**b**) and (**c**) is nearly one indicating diffusive behavior

uniform. Notably, the effect of non-zero K is dramatic only for the stationary case: from no cross-gyre mixing at $K = 0$, to mixing between the gyres for any positive K.

We show the PDF of the RD (Figs. 3, 4, column III) and the kurtosis of the RD (Fig. 5a) to quantify changes in the RD field with increasing K. For $K = 0$ the PDF has one large peak near zero and a long tail (Figs. 3, 4, panel IIIa). The large peak corresponds to "elliptic type" trajectories that are relatively stable, having a low, nearly zero, RD. The tail corresponds to the much smaller set of "hyperbolic type" trajectories that have high RD due to their

proximity to exponential instabilities. As K increases, the main peak shifts to the right until the PDF is characterized by a wide peak with non-zero mean that depends on K.

The influence of increased K on the mixing barriers, namely the tail of the PDF, is quantified by computing the kurtosis of the RD for each K. Twenty simulations were conducted for each K and the ensemble mean kurtosis and standard deviation are presented for both the stationary (dashed red) and time-periodic (solid blue) cases in Fig. 5a. In both cases the large kurtosis at small K is due to the presence of mixing barriers (characterized by large RD). In contrast, at high values of K, the kurtosis is smaller, indicating a more evenly distributed RD. Unlike the time-periodic case, the kurtosis of the RD in the stationary case (dashed red line) is non monotonic in K.

This distinct dependence on K may be explained by the dynamical differences between the two cases. Particle trajectories in the stationary double gyre without diffusion ($K = 0$) move along the streamlines of the flow and, therefore, there is no mixing at all between the two gyres [48]. In this stationary non-diffusive case, the RD of almost all particles grows linearly with time by the shear between different streamlines and only the particles that are closest to the separating line between the gyres experience larger RD. Thus, the kurtosis of the RD reflects the impact of this very small exceptional set. Introducing even the smallest value of the eddy diffusivity leads to a dramatic effect: particles can hop from one gyre to the other, thus dramatically increasing the number of neighboring particles that split between the two gyres. For a given integration time, the number of particles separated by this mechanism increases with increasing K, thus the kurtosis initially increases monotonically in Fig. 5. At larger values of K, diffusion dominates and the large-scale circulation (i.e., the double gyres) has little influence on particle trajectories, leading to a decrease of the kurtosis. In contrast, chaotic mixing between the gyres occurs even when $K = 0$ in the time-periodic, or unsteady gyres, and particles contained in the chaotic region, move back and forth between the gyres in a complicated fashion [41,48]. Therefore, small eddy diffusivity has a relatively mild effect, mainly to smooth the distribution of the RDs and to lower the kurtosis. We propose that the difference between the effects of the eddy diffusivity on stationary versus time-dependent flows is nicely reflected by the dependence of the kurtosis on K shown in Fig. 5.

4.2 Identifying the upper bound of **K**

We assert that the value of K that corresponds to the transition of the kurtosis towards its minimum value represents the eradication of the mixing barriers by the eddy diffusivity. While we cannot define a specific and sharp cut-off value of the kurtosis that demonstrates the lack of barriers, the sharp drop followed by a leveling of the kurtosis suggests that the barriers disappear. We suggest that this transition corresponds to the upper bound for the eddy diffusivity K for this flow field. The transition in the time-periodic case occurs around $K = 10^{-3}$, and at $K = 10^{-2}$ in the stationary case. While the evaluation of the transition is somewhat subjective, Fig. 5a suggests that the upper bound of the time-periodic double gyre is approximately one order of magnitude less than the stationary double gyre, regardless of the specific cut-off criteria for the kurtosis leveling.

Figure 5 also shows the logarithm of the domain averaged RD^2 for the time-periodic double gyre (b) and the stationary double gyre (c) as a function of time (the four curves in (b) and (c) correspond to the four values of K shown in Figs. 3 and 4). For small K (i.e., $K = 0$ and $K = 10^{-5}$) the averaged behavior is sub-diffusive for small t and exponential for large t, while for large K (i.e, $K = 10^{-3}$ and $K = 10^{-2}$) the behavior is diffusive. While there is a clear transition between the curves computed for different K, this representation

shows little difference between the time-dependent and stationary double gyres. The combined information from Figs. 3, 4 and 5a, demonstrate that while there are clear differences between the barriers of the stationary and time-dependent flows, the average, or first moment, is not sensitive enough to distinguish between them.

Finally, one may suspect that selecting K such that the stochastic component and the large-scale flow have equal magnitudes can provide an estimate of the upper bound of the eddy diffusivity in a given flow field. However, this does not appear to be the case in the time-periodic double gyre example. The mean amplitude of the stochastic term first exceeds the amplitude of the large scale flow at $K = 10^{-2}$ while our results indicate that the upper bound for K in the time-dependent double gyre is at least an order of magnitude less. Thus, the upper bound of the eddy diffusivity cannot be determined simply by comparing the magnitudes of the large scale flow and of the stochastic component.

5 Geophysical application: the gulf of Eilat

The northern terminus of the Gulf of Eilat (hereafter 'the gulf') is a nearly rectangular, deep ($\sim$700 m), and semi-enclosed basin in the northeast region of the Red Sea. The circulation in the Gulf has tidal [49], thermohaline [50,51], and wind-driven [52] components. Coherent eddies with lifetimes $\sim$O (24 h) are observed sporadically during winter [53]. Submesoscale flow features, such as barriers to mixing have also been observed [35].

Two 42 MHz SeaSonde HF radar systems have been operational in the northwestern gulf near the city of Eilat, Israel since August 2005. As with any remote-sensing observation system, there are gaps and outliers in the HF radar data that require post-processing. The open boundary modal analysis (OMA) of Lekien et al. [54] is applied to raw HF radar data to yield the spatially interpolated and filtered velocity on a regularly spaced grid (300 m resolution) with a time step of 30 min, as detailed in Lekien and Gildor [55]. These velocities were used to calculate the trajectories of particles using the forward Euler–Maruyama method with a time step of 10 min (integrations using different time steps and solvers show similar results). The RD was computed from the end points of the particle trajectories; however, particles that exited the domain either through the open boundaries or through stochastic jumps onto land were removed from the simulation.

Figure 6 shows aerial photographs of a rare flood that introduced sediments to the normally clear waters of the Gulf of Eilat. Panel (a) shows the sharp front between the muddy and clear water right after the flood on 3 February 2006. Panel (b) shows the existence of the front two days later (taken from a different angle). This sharp front was located approximately along the barrier identified by the calculation of the RD based on HF radar measurements of surface currents shown in Fig. 7 [35]. The existence of the sharp front even two days after the start of the flood demonstrates that mixing was in homogeneous and relatively weak across the barrier. In the absence of a barrier, the interface between the muddy freshwater and relatively clear seawater would not have remained so sharp.

Column I of Fig. 7 shows the spatial distribution of the RD after 13 h of integration starting 3 February 2006 at 05:00 GMT (within the same time period analyzed in Gildor et al. [35]). The RD is far from uniform. Notably, in Panel Ia of Fig. 7, a barrier shown by the brightly colored line, starting in the northwestern corner of the gulf and ending at the middle of the east coast, can be seen. Particles released in the white area exited the domain and their RD could not be calculated.

The RD plots in Fig. 8 show that barriers still exist when the spatial resolution is reduced to 600 m (top panel) and when the temporal resolution is decreased to 1 h (bottom panel).

Fig. 6 A barrier to mixing as shown by *aerial photographs* illustrating that the sediments do not mix beyond the same barrier that was calculated using surface currents observed by HF radar. The *top panel* (**a**) was taken 3 February 2006 from the northwestern corner of the gulf facing southeast. The *bottom panel* (**b**) was taken facing northwest on 5 February 2006, 2 days after the flood. The *green rectangles* mark the same location. Photos by Dubi Tal, Albatross Photography

While the exact location and details of the barriers are somewhat different, the main features are similar, indicating that the existence of the barriers is not too sensitive to the temporal resolution or the coarseness of the grid (as expected from theoretical grounds [38]). The existence and detection of this barrier enables us to assign an upper bound to the eddy diffusivity as described in Sect. 4.

Panel Ib of Fig. 7 shows that the mixing barrier weakens as K increases to $0.1\,\mathrm{m^2\,s^{-1}}$. The mixing barrier is still present at $K = 1\,\mathrm{m^2\,s^{-1}}$ (panel Ic) but is difficult to distinguish. At $K = 10\,\mathrm{m^2\,s^{-1}}$ (not shown), 90% of the particles leave the domain. Example particle trajectories (Fig. 7, column II) illustrate the random spread of particle paths and the degradation of the barriers as the eddy diffusivity increases. The PDFs (column III of Fig. 7) of the RD for increasing K are similar to those shown in Figs. 3 and 4. The kurtosis is plotted as a function of K in Fig. 9. Panel (b) of Fig. 9 shows the time evolution of the logarithm of the mean RD^2 of particles in the Gulf of Eilat for a given value of K. For small K (i.e., $K = 0$–$1\,\mathrm{m^2\,s^{-1}}$) the averaged behavior is sub-diffusive for small t and exponential for large t, while for large K (i.e, $K = 10\,\mathrm{m^2\,s^{-1}}$ and $K = 100\,\mathrm{m^2\,s^{-1}}$) the behavior is diffusive. The kurtosis drops sharply for $K > 10^{-1}$ and is lower than 6 for $K = 2$, much less than 21 for $K = 0$. Therefore, we estimate the upper bound for K to be between 1 and $10\,\mathrm{m^2\,s^{-1}}$.

Other estimates for this region (e.g. from dye release experiments) do not exist, largely due to the current geo-political situation. Yet, this value is not far from the diffusivity of $2\,\mathrm{m^2\,s^{-1}}$ at scales of 1–10 km in the eastern North Atlantic estimated by Ledwell et al. [14] and 0.3–$4.9\,\mathrm{m^2\,s^{-1}}$ computed by Sundermeyer and Ledwell [15] on a continental shelf. Simple dimensional analysis yields a wider range of possible values for K in the Gulf of Eilat. A typical velocity scale $U = 0.1\,\mathrm{ms^{-1}}$ and a typical length scale L between 10^2 (width of the barrier) and 10^3 m (10 % of the length of the domain), yield a wide range of estimates of

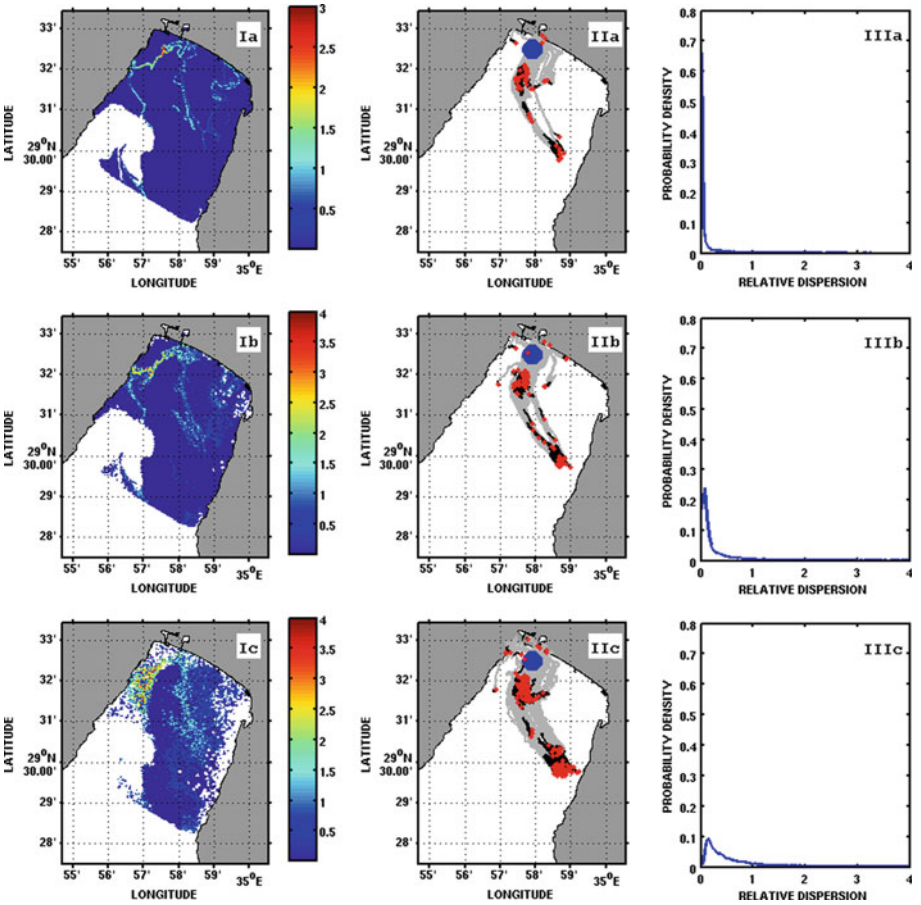

Fig. 7 Similar to Figs. 3 and 4, the RD, particle trajectories and PDFs are shown for real observations from the Gulf of Eilat. Row (a) represents the deterministic case, i.e. $\mathbf{u}' = 0$. Rows (b) and (c) show results for $K = 0.1$ and $1\,\mathrm{m^2\,s^{-1}}$, respectively. *Column I* The mixing barrier is indicated by high values of the RD (corresponding to contours of *warm colors* indicated by the *red arrows*) and its erosion is evident as K increases. The *green rectangles* correspond to the same location marked in Fig. 6. The *white areas* indicate particles that exited the domain and, therefore, provide no data. *Column II* Particle trajectories begin at the *blue circles*. The *gray lines* represent the trajectory, the *black lines* represent the final six positions, and the *red dots* indicate the final position. *Column III* PDFs of the RD (*right column*) show the broadening of the peak as the RD becomes more spatially uniform with increasing K

the eddy diffusivity ($K = UL = 10$–$100\,\mathrm{m^2\,s^{-1}}$). It is not known a priori which length-scale should be used and this simple calculation demonstrates the scale-dependence of the eddy diffusivity.

6 Sensitivity tests

An extensive set of sensitivity tests were performed to evaluate the robustness of our method in the double gyre model. We briefly describe the sensitivity of the results to the number of seeded particles, choice of the noise distribution, and to the total integration time.

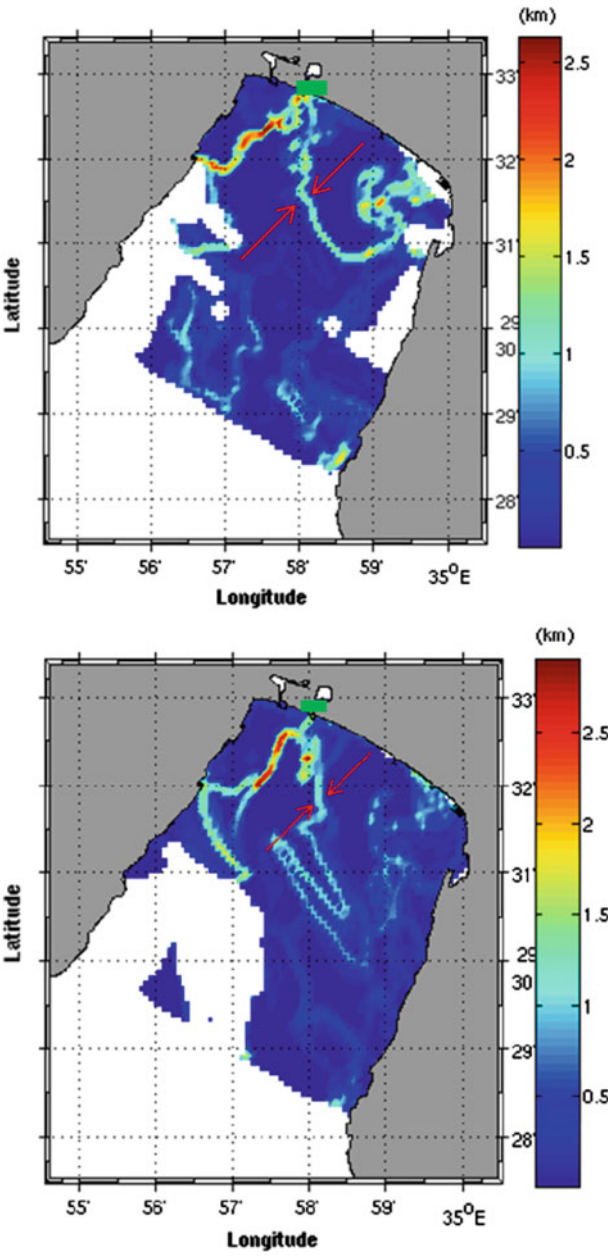

Fig. 8 The RD still captures the presence of mixing barriers (*red arrows*) despite decreased spatial (*top*) and temporal resolution (*bottom*). In the *top panel* the spatial resolution was decreased to 600 m. The temporal resolution in the *bottom panel* was reduced to 1 h. The *green rectangles* correspond to the same location marked in Fig. 6

A sufficient number of particles are required to identify the existence of the barriers and to reliably estimate the width of the barrier (the calculation of the kurtosis of the RD at small K requires adequate resolution of the barrier). Figure 10 shows how the width of the barrier

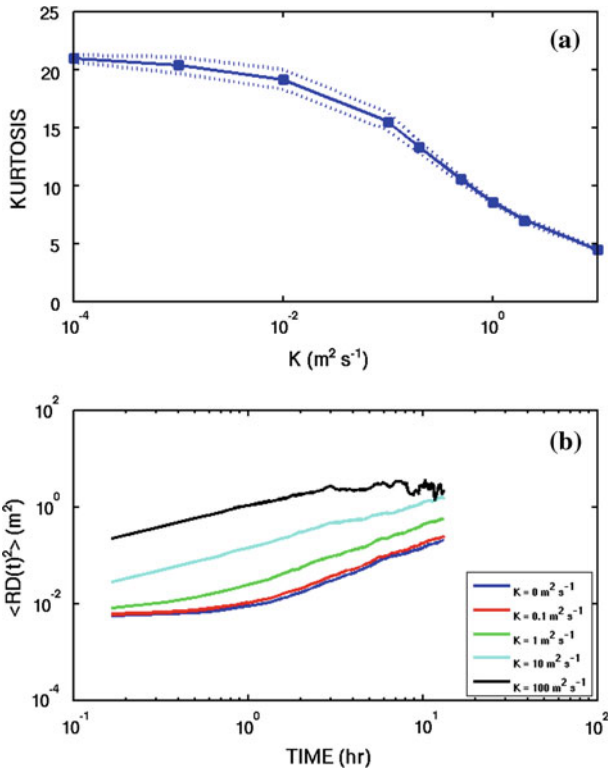

Fig. 9 **a** The kurtosis of the RD in the geophysical example of the Gulf of Eilat is plotted as a function of the eddy diffusivity K. **b** The logarithm of the domain averaged RD^2 as a function of time for given K (corresponding to the three values of K shown in Fig. 7). Similar to Fig. 5b–c, the slope of the two *upper curves* is nearly one indicating diffusive behavior

(based on the derivative of the RD) decreases with increasing particle density (decreasing grid size). The results are not sensitive to grid sizes smaller than 0.01. As a compromise between nearly constant barrier width and computation time, the results presented in this paper use a grid spacing of 0.005 in both x and y. This grid spacing corresponds to an initial grid of 400×200 particles (red square in Fig. 10). Similarly, the results from the Gulf of Eilat were not sensitive to the grid spacing (for grids of 100×100, 200×200, and 300×300 particles).

The sensitivity of our stochastic model to the distribution of the noise used to define w in (13) was tested by defining w as a uniformly distributed random variable. The results were not affected (as suggested by Hathorn [56]) and the same upper bound was deduced. Hathorn [56] reviews the applicability of several statistical distributions in the random walk model.

In the double gyre example, integration over a shorter time interval ($t = [0, 10]$) shows that the response of the kurtosis of the RD computed for small K is somewhat different but the sharp decrease and, specifically, the inferred upper bound do not change. Additional tests show no sensitivity to time steps $dt < 0.1$.

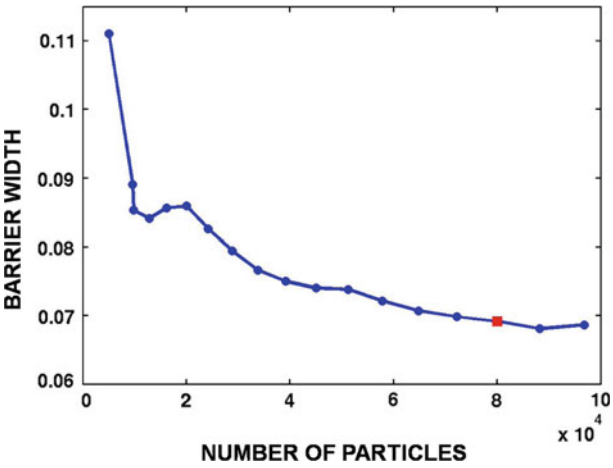

Fig. 10 The average non-dimensional width of the mixing barrier of the time-dependent double gyre for $K = 10^{-10}$ as a function of increasing particle density. The average width of the mixing barrier was computed over the sub-domain $[0.9, 1.2] \times [0.1, 0.3]$. The width decreases and approaches a constant value as the number of particles seeded in the domain increases. Particles are distributed evenly over the domain to maintain constant grid spacing. The *red square* indicates the number of particles used in all the computations presented in this paper (400×200)

7 Discussion

7.1 Diffusivity, chaotic mixing, and zeroth-order stochastic model

The mixing that occurs through the motion of "sub-grid-scale" eddies is traditionally modeled by the tracer advection-diffusion equation (see e.g. Tel et al. [57]):

$$\frac{DC}{Dt} = \frac{\partial C}{\partial t} + \vec{U}_{LS}(\vec{x}, t)\frac{\partial C}{\partial x} = \nabla(\vec{K}(\vec{x}, t)\nabla C) \tag{14}$$

where C represents a tracer, $\mathbf{U}_{LS}$ represents the large-scale advection term, K is the eddy diffusivity vector, and $\frac{D}{Dt}$ indicates the material derivative. The reasoning behind the introduction of a diffusion term with an enhanced diffusion coefficient K is similar to the reasoning employed in the use of an "eddy viscosity" in numerical models to achieve closure and numerical stability. Thus, (14) represents the mixing of some distribution of a tracer due to the combined effect of large scale flow and the sub-grid-scale eddies that randomly move from one place to another. It is well established that the modeling of the large scale flow influences the fitting of the diffusion coefficient K to real data (see Ridderinkhof and Zimmerman [33], LaCasce [45] and Fig. 5). In particular, modeling the large scale flow by a constant $\mathbf{U}_{LS}$ and a constant K makes (14) too simplistic in real geophysical applications.

One approach to make (14) applicable to complex real-life applications is to take $\mathbf{U}_{LS}$ to be stationary and fit spatially and/or temporally varying K (which can be a vector that reflects non-isotropic effects) to the data. This approach is called the "zeroth-order" stochastic model in the review by LaCasce [45]. Namely, in this approach, the complex mixing pattern of the tracer field is modeled by the spatial and temporal variability of the eddy diffusivity, K. Comparison of Figs. 3 and 4 demonstrates that the differences in mixing between the stationary and the time-periodic flows cannot be overcome simply by adding a uniform diffusion coefficient. Thus, in the stationary large-scale flow approach, K must have a non-trivial form

[3] and may, for example, be represented by an operator that depends on the local behavior of the large scale tracer or velocity field, as suggested by Smagorinsky [58] or Leith [59].

An implicit assumption in (14) is that the fluctuations of the velocity about the large scale flow are random. Previous studies of meso-scale oceanic flows showed that the distribution of the fluctuations about a stationary large scale flow is not Gaussian [12]. These observations led to the development of higher-order stochastic models [45].

The present study uses (14) with a spatially and temporally varying large scale flow where K is taken to be isotropic and either zero or constant. This non-stationary zeroth-order model is widely used in oceanography and limnology [5–11]. We have seen that in flows that exhibit chaotic advection at $K = 0$, the effects of small diffusivity or small uncertainties in $\mathbf{U}_{\mathrm{LS}}$ on the mixing are not dramatic (see Figs. 5, 9). Indeed, the resulting mixing patterns that are dominated by chaotic advection are believed to capture the main mixing characteristics of oceanic flows [33,36,38,48]. We have also demonstrated that if the large scale flow is adequately resolved, the barriers are robust (see Fig. 8) and the destruction of the barrier by the eddy diffusivity is insensitive to the noise distribution (see Sect. 6) and to the uncertainties (namely the fine resolution) in the large scale flow. Thus, we propose that the non stationary zeroth-order stochastic model with constant K can be used when using time-dependent, spatially varying large-scale flow if the temporal and spatial resolution adequately resolves the mixing barriers.

Furthermore, we claim that the high spatial and temporal resolutions of the observed velocities in the Gulf of Eilat adequately resolve sub-mesoscale flow features [35], and, therefore, that the non-stationary zeroth-order stochastic model is suitable. To substantiate this claim, we examine the fluctuations of the observed velocity about the large scale flow at various resolutions. Figure 11 shows four different PDFs of velocity fluctuations calculated in four different ways. The y-axes of the PDFs are plotted on a logarithmic scale to emphasize the behavior of the tails. The tails of the PDFs are linear, indicative of exponential decay. Thus, the PDFs show that the probability is highest around zero and decays exponentially at larger values.

Panels (a) and (b) illustrate the sensitivity of the PDFs of the fluctuations to different spatial resolutions. To compute the fluctuations, the mean velocities on the coarse resolution grid were subtracted from the original data (i.e., the original data points located inside the corresponding coarse grid cell). The original temporal resolution (30 min) was not changed in (a) and (b). The PDFs shown in (b) describe velocity fluctuations computed by averaging the original high resolution (300 m) data to obtain a coarse resolution (1.2 km) grid. Panel (a) shows the PDFs computed using the same process but with a 600 m grid. Comparing (a) and (b), we see that the PDFs in (b) are asymmetric while the PDFs in (a) are symmetric. The asymmetry seen in (b) implies that decreased spatial resolution introduces a directional preference. Conversely, the symmetric PDFs in (a) indicate that spatial resolutions of 600 m or higher adequately resolve the flow and that the non-stationary zeroth order model may be suitable.

Panels (c) and (d) illustrate the sensitivity of the PDFs to two different temporal resolutions. The original spatial resolution of 300 m was unchanged in both (c) and (d). Instead, the original data were averaged in time to produce coarser temporal resolutions. The means of the coarser temporal resolution data were subtracted from the original data to obtain the fluctuations. Panel (c) shows the PDFs of the velocity fluctuations when the temporal resolution is decreased to 1 h. Panel (d) shows the PDFs of the velocity fluctuations when the temporal resolution is decreased to 4 h. The PDFs in (d) are asymmetric indicating directional preference at lower (4 h) temporal resolution. The PDFs in (c) are symmetric indicating that, at high enough resolution (1 h or higher), the fluctuations have no directional preference and

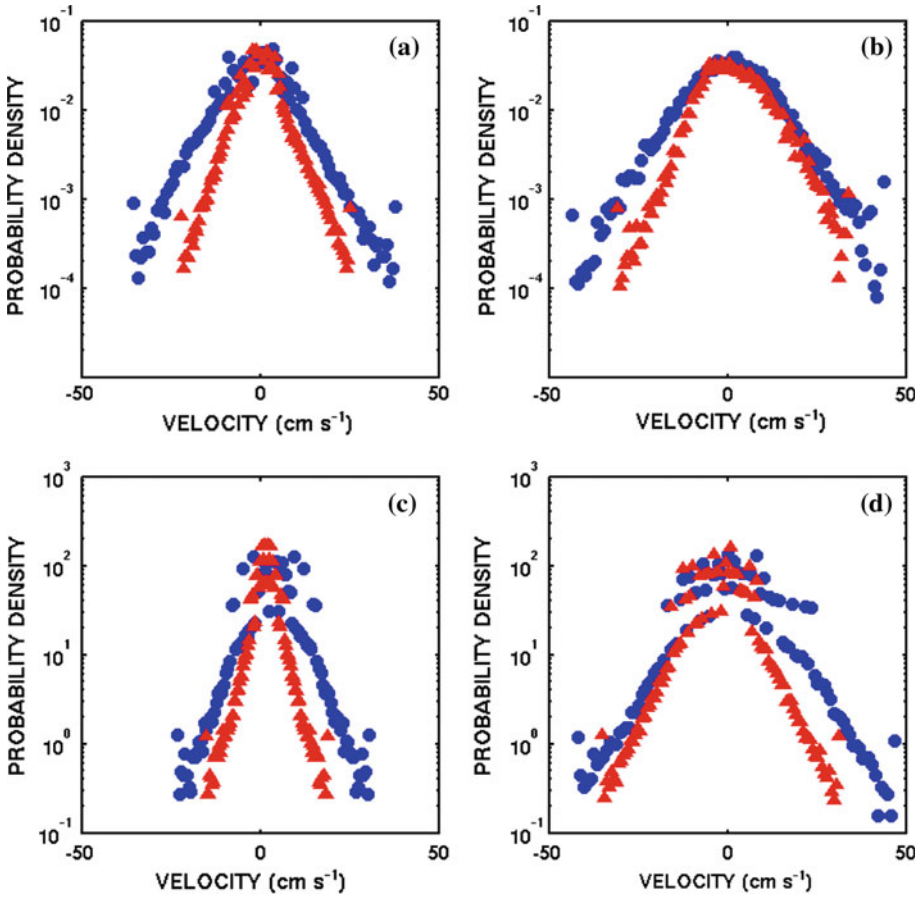

Fig. 11 The PDFs of the zonal (*blue circles*) and meridional (*red triangles*) velocity fluctuations for different spatial and temporal averaging schemes in the Gulf of Eilat. In **a–b** the spatial resolution was reduced to 600 and 1,200 m, respectively. **c–d** show the PDFs of the fluctuations for temporal resolutions of 1 and 4 h, respectively. The *y*-axis is plotted on a logarithmic scale

that the zeroth order model should be suitable. Overall, Fig. 11 shows that the use of the zeroth order model is acceptable with velocities observed at a spatial resolution of 300 m and a temporal resolution of 30 min. Moreover, Fig. 11 suggests that the use of a stationary zeroth order model is not justified as the asymmetry in the fluctuations at lower temporal and spatial resolution is apparent.

7.2 Limitations and future directions

The stochastic Lagrangian model used in this study assumed constant K. Namely we assumed that the fluctuations about the large scale flow are uniform throughout the domain. For a small domain and limited periods, this assumption is probably reasonable, however in a large domain or over longer periods, K may need to be spatially dependent. Indeed, some general circulation and particle tracking models employ both time-dependent velocity fields and spatially varying eddy diffusivity [60,61]. In situations where the

use of spatially varying eddy diffusivity is warranted, our estimate of the upper bound of K is likely to be relevant only in the vicinity of the observed barrier.

Our method suggests that the upper bound of the eddy diffusivity can be determined by examining how the RD changes with increasing K. We propose that the upper bound of K is located within the regime where the sharp drop in the kurtosis of the RD ends. However, a general theory to evaluate the existence of mixing barriers and their dependence on time and the behavior of the large scale flow does not exist yet. Additional studies may provide a refinement and perhaps sharper criteria for quantifying the eradication of mixing barriers.

Other methods have been proposed to estimate the mixing efficiency of passive tracers with non-trivial spatial dependence of the diffusion term. For example, Nakamura [37,62] proposed the use of tracer contours as new coordinate systems and to calculate the flux and diffusion across these contours. The "effective diffusivity" introduced in this system is quite different from the "eddy diffusivity" of (14). It would be an interesting problem to relate these concepts to simulations of particle trajectories in which there is no obvious measure for the "concentration" of particles.

Comparing the zeroth-order (random walk) and first-order (random flight) models, Ullman et al. [46] find that the first-order model produces better results in search and rescue applications when the same dispersion coefficient, that is found by parameterization of extensive drifter experiments, is used in both models. The relation between these results and the current work deserve a separate study. On one hand, it is unclear how the existence of Lagrangian barriers influences the comparison between the two models. On the other hand, the current approach of estimating an upper bound to the horizontal eddy diffusivity may be possibly extended to a first-order model.

8 Conclusions

We propose a method to estimate the upper bound of the horizontal eddy diffusivity in the presence of mixing barriers using a non-stationary zeroth-order stochastic Lagrangian particle tracking model. The combination of the visual examination of the RD field and the calculation of the kurtosis of the RD allows us to estimate the magnitude of the eddy diffusivity that results in the eradication of the mixing barrier. We propose that the value of the eddy diffusivity that eradicates the observed mixing barrier represents an upper bound on the actual eddy diffusivity. Our proposed method is demonstrated using a simplistic double gyre model and on observed surface currents from the Gulf of Eilat.

Acknowledgements This research was supported by NATO SfP982220 and by The Israel Science Foundation (grant No. 1344/09). HG is the Incumbent of the Rowland and Sylvia Schaefer Career Development Chair and is supported by a research grant from the Estate of Sanford Kaplan. VRK is the Estrin Family Professor of Computer Science and Applied Mathematics and acknowledges support by the Minerva foundation. The Port in Eilat allowed us to install one of the HF radar sites on its property. Airspan provides the wireless communication between the radar sites. We thank the management and the staff of the Inter-University Institute for Marine Sciences of Eilat (IUI) for their cooperation and help. We thank two anonymous reviewers for greatly improving our manuscript.

References

1. Stommel H (1949) Horizontal diffusion due to oceanic turbulence. J Mar Res 13:199–225
2. Burchard H, Bolding K (2001) Comparative analysis of four second-moment turbulence closure models for the oceanic mixed layer. J Phys Oceanogr 31:1943–1967

3. Majda AJ, Kramer PR (1999) Simplified models for turbulent diffusion: theory, numerical modeling, and physical phenomena. Phys Rep 314:237–574
4. Ross ON, Sharples J (2004) Recipe for 1-D Lagrangian particle tracking models in space-varying diffusivity. Limnol Oceanogr Methods 2:289–302
5. Rueda FJ, Schladow SG, Clark JF (2008) Mechanisms of contaminant transport in a multi-basin lake. Ecol Appl 18:A72–A87
6. Chen W, Liu W, Kimura N, Hsu M (2009) Particle release transport in Danshuei River estuarine system and adjacent coastal ocean: a modeling assessment. Environ Monit Assess. doi:10.1007/s10661-009-1123-2
7. Marinone SG, Ulloa MJ, Parés-Sierra A, Lavín MF, Cudney-Bueon R (2008) Connectivity in the northern Gulf of California from particle tracking in a three-dimensional numerical model. J Mar Syst 71:149–158
8. Tilburg CE, Reager JT, Whitney MM (2005) The physics of blue crab larvae recruitment in Delaware Bay: a model study. J Mar Res 63:471–495
9. Xue H, Incze L, Xu D, Wolff N, Pettigrew N (2008) Connectivity of lobster (*Homarus americanus*) populations in the coastal Gulf of Maine: part I: circulation and larval transport potential. Ecol Model 210:193–211
10. Incze L, Xue H, Wolff N, Xu D, Wilson C, Steneck R, Wahle R, Lawton P, Pettigrew N, Chen Y (2010) Connectivity of lobster (*Homarus americanus*) populations in the coastal Gulf of Maine: part II. Coupled biophysical dynamics. Fish Ocean 19:1–20
11. Blumberg AF, Dunning DJ, Li H, Heimbuch D, Geyer WR (2004) Use of a particle-tracking model for predicting entrainment at power plants on the Hudson River. Estuaries 27:515–526
12. Davis RE (1991) Observing the general circulation with floats. Deep Sea Res 38:531–571
13. Bogucki DJ, Jones BH, Carr M (2005) Remote measurements of horizontal eddy diffusivity. J Atmos Ocean Technol 22:1373–1380
14. Ledwell JR, Watson AJ, Law CS (1998) Mixing of a tracer in the pycnocline. J Geophys Res 103(C10):21,499–421,529
15. Sundermeyer MA, Ledwell JR (2001) Lateral dispersion over the continental shelf: analysis of dye release experiments. J Geophys Res 106(C5):9603–9621
16. List J, Gartrell G, Winant CD (1990) Diffusion and dispersion in coastal waters. J Hydraul Eng 116: 1158–1179
17. Sanderson BG, Booth DA (1991) The fractal dimension of drifter trajectories and estimates of horizontal eddy-diffusivity. Tellus 43A:334–349
18. Zhurbas V, Sang Oh I (2003) Lateral diffusivity and Lagrangian scales in the Pacific Ocean as derived from drifter data. J Geophys Res. doi:10.1029/2002JC001596
19. Kawabe M (2008) Vertical and horizontal eddy diffusivities and oxygen dissipation rate in the subtropical northwest Pacific. Deep Sea Res I 55:247–260
20. Haller G, Yuan G (2000) Lagrangian coherent structures and mixing in two-dimensional turbulence. Phys D 147:352–370
21. Haller G (2001) Lagrangian structures and the rate of strain in a partition of two-dimensional turbulence. Phys Fluids 13:3365–3385
22. Lipphardt BL, Small G, Kirwan AD, Wiggins S, Ide K, Grosch CE, Paduan JD (2006) Synoptic Lagrangian maps: application to surface transport in Monterey Bay. J Mar Res 64:221–247
23. Olascoaga MJ, Rypina II, Brown MG, Beron-Vera FJ, Kocak H, Brand LE, Halliwell GR, Shay LK (2006) Persistent transport barrier on the west Florida shelf. Geophys Res Lett. doi:10.1029/2006GL027800
24. Boffetta G, Lacorata G, Radaelli G, Vulpiani A (2001) Detecting barriers to transport: a review of different techniques. Phys D 159(1–2):58–70
25. Berloff PS, McWilliams JC, Bracco A (2002) Material transport in oceanic gyres. Part I: Phenomenology. J Phys Oceanogr 32:764–796
26. Shadden SC, Lekien F, Marsden JE (2005) Definition and properties of Lagrangian coherent structures from finite-time Lyapunov exponents in two-dimensional aperiodic flows. Phys D 212:271–304
27. Orre S, Gjevik B, Lacasce JH (2006) Characterizing chaotic dispersion in a coastal tidal model. Cont Shelf Res 26:1360–1374
28. d'Ovidio F, Fernandez V, Hernandez-Garcia E, Lopez C (2004) Mixing structure in the Mediterranean Sea from finite-size Lyapunov exponents. Geophys Res Lett. doi:10.1029/2004GL020328
29. Lehahn Y, d'Ovidio F, Levy M, Heifetz E (2007) Stirring of the northeast Atlantic spring bloom: a Lagrangian analysis based on multisatellite data. J Geophys Res. doi:10.1029/2006JC03927
30. Waugh DW, Abraham ER, Bowen MM (2006) Spatial variations of stirring in the surface ocean: a case study of the Tasman Sea. J Phys Oceanogr 36:526–542
31. Garcia-Olivares A, Isern-Fontanet J, Garcia-Ladona E (2007) Dispersion of passive tracers and finite-scale Lyapunov exponents in the Western Mediterranean Sea. Deep Sea Res 54:253–268
32. Samelson R (1992) Fluid exchange across a meandering jet. J Phys Oceanogr 22:431–440

33. Ridderinkhof H, Zimmerman J (1992) Chaotic stirring in a tidal system. Science 258:1107–1111
34. Joseph B, Legras B (2002) Relation between kinematic boundaries, stirring, and barriers for the Antarctic polar vortex. J Atmos Sci 59:1198–1212
35. Gildor H, Fredj E, Steinbuck J, Monismith S (2009) Evidence for submesoscale barriers to mixing in the ocean from current measurements and aerial photographs. J Phys Oceanogr 39:1975–1983
36. Lekien F, Coulliette C, Mariano AJ, Ryan EH, Shay LK, Haller G, Marsden J (2005) Pollution release tied to invariant manifolds: a case study for the coast of Florida. Phys D 210:1–20
37. Nakamura N (2008) Quantifying inhomogeneous, instantaneous, irreversible transport using passive tracer field as a coordinate. Lect Notes Phys 744:137–164
38. Haller G (2002) Lagrangian coherent structures from approximate velocity data. Phys Fluids 14: 1851–1861
39. Lichtenberg AJ, Lieberman MA (1992) Regular and chaotic dynamics, 2nd edn, Applied Mathematical Sciences, vol 38. Springer, New York
40. Wiggins S (2005) The dynamical systems approach to Lagrangian transport in oceanic flows. Annu Rev Fluid Mech. doi:10.1146/annurev.fluid.37.061903.175815
41. Koshel KV, Prants SV (2006) Chaotic advection in the ocean. Phys-Uspekhi. doi:10.1070/PU2006v049nl1ABEH006066
42. Garrett C (2006) Turbulent dispersion in the ocean. Prog Oceanogr 70:113–125
43. Bauer S, Swenson MS, Griffa A, Mariano AJ, Owens K (1998) Eddy-mean flow decomposition and eddy-diffusivity estimates in the tropical Pacific Ocean, 1. Methodology. J Geophys Res 103:30855–30871
44. Pedlosky J (1987) Geophysical fluid dynamics. Springer, New York
45. LaCasce JH (2008) Statistics from Lagrangian observations. Prog Oceanogr 77:1–29
46. Ullman DS, O'Donnell J, Kohut J, Fake T, Allen A (2006) Trajectory prediction using HF radar surface currents: Monte Carlo simulations of prediction uncertainties. J Geophys Res. doi:10.1029/2006JC003715
47. Gard TC (1988) Introduction to stochastic differential equations, pure and applied mathematics, vol 114. Marcel Dekker, New York
48. Yang H, Liu Z (1994) Chaotic transport in a double gyre ocean. Geophys Res Lett 21:545–548
49. Monismith SG, Genin A (2004) Tides and sea level in the Gulf of Aqaba (Eilat). J Geophys Res. doi:10.1029/2003JC002069
50. Biton E, Silverman J, Gildor H (2008) Observations and modeling of a pulsating density current. Geophys Res Lett. doi:10.1029/2008GL034123
51. Monismith SG, Genin A, Reidenbach MA, Yahel G, Koseff JR (2006) Thermally driven exchanges between a coral reef and the adjoining ocean. J Phys Oceanogr 36:1332–1347
52. Berman T, Paldor N, Brenner S (2000) Simulation of wind-driven circulation in the Gulf of Elat (Aqaba). J Mar Syst 26:349–365
53. Gildor H, Fredj E, Kostinski A (2010) The Gulf of Eilat/Aqaba: a natural driven cavity? Geophys Astron Fluid Dyn. doi:10.1080/03091921003712842
54. Lekien, F, Coulliette C, Bank R, Marsden J (2004) Open-boundary modal analysis: interpolation, extrapolation, and filtering. J Geophys Res. doi:10.1029/2004JC002323
55. Lekien F, Gildor H (2009) Computation and approximation of the length scales of harmonic modes with application to the mapping of surface currents in the Gulf of Eilat. J Geophys Res. doi:10.1029/2008JC004742
56. Hathorn WE (1996) A second look at the method of random walks. Stoch Hydrol Hydraul 10:319–329
57. Tel T, de Moura A, Grebogi C, Karolyi G (2005) Chemical and biological activity in open flows: a dynamical system approach. Phys Rep 413:91–196
58. Smagorinsky J (1963) General circulation experiments with the primitive equations I: the basic experiment. Mon Weather Rev 91:99–164
59. Leith CE (1996) Large eddy simulation of complex engineering and geophysical flows. Phys D 98: 481–491
60. Figueroa HA, Olson DB (1994) Eddy resolution versus eddy diffusion in a double gyre GCM. Part I: the Lagrangian and Eulerian description. J Phys Oceanogr. doi:10.1016/j.dsr.2006.10.009
61. Hunter JR, Craig PD, Phillips HE (1993) On the use of random walk models with spatially variable diffusivity. J Comput Phys 106:366–376
62. Nakamura N (1996) Two-dimensional mixing, edge formation, and permeability diagnosed in an area coordinate. J Atmos Sci 53:1524–1537